

Nanoscale Resistive Switching in Amorphous Perovskite Oxide (a -SrTiO₃) Memristors

Hussein Nili,* Sumeet Walia, Sivacarendran Balendhran, Dmitri B. Strukov, Madhu Bhaskaran, and Sharath Sriram*

M.B. and S.S. dedicate this work to the memory of Dr. K. Govindarajan

Memristive devices are the precursors to high density nanoscale memories and the building blocks for neuromorphic computing. In this work, a unique room temperature synthesized perovskite oxide (amorphous SrTiO₃: a -STO) thin film platform with engineered oxygen deficiencies is shown to realize high performance and scalable metal-oxide-metal (MIM) memristive arrays demonstrating excellent uniformity of the key resistive switching parameters. a -STO memristors exhibit nonvolatile bipolar resistive switching with significantly high (10^3 – 10^4) switching ratios, good endurance ($>10^6$ I – V sweep cycles), and retention with less than 1% change in resistance over repeated 10^5 s long READ cycles. Nano-contact studies utilizing in situ electrical nanoindentation technique reveal nanoionics driven switching processes that rely on isolatedly controllable nano-switches uniformly distributed over the device area. Furthermore, in situ electrical nanoindentation studies on ultrathin a -STO/metal stacks highlight the impact of mechanical stress on the modulation of non-linear ionic transport mechanisms in perovskite oxides while confirming the ultimate scalability of these devices. These results highlight the promise of amorphous perovskite memristors for high performance CMOS/CMOL compatible memristive systems.

1. Introduction

Memory technologies were traditionally utilized to store digital data in the form of “1”s and “0”s. Current interest lies in technologies which enable analog memories that have multiple states. This enables unprecedented high density memories and most significantly neuromorphic computing.^[1] These rely on the electronic state of memories being highly non-volatile, with durable and cyclic switching, and easy differentiation of ON/

OFF states. Nanoscale resistive memories (or “memristors”) satisfy many of these requirements, and are reliant on functional oxides. They are normally configured as passive two terminal metal-insulator-metal (MIM) devices based on functional binary and ternary metal-oxides (e.g., TiO₂, SrTiO₃). These offer a scalable, fast, non-volatile and low energy “memristive” performance.^[1,2] Their dynamic non-linear current–voltage characteristics also suggest applications in non-linear circuit design and alternative logic architectures.^[1b,2b,3]

The bipolar resistive switching behaviour in these devices is attributed to a combination of electronic effects at the metal/oxide interfaces and reversible redox reactions and nanoionics transport in transition metal-oxide layers.^[2c–f,4] These processes are triggered in the oxide upon the creation of extended defect structures during an electroforming process, under high electrical gradients. However, the underlying microscopic conduction and

switching mechanisms strongly depend on the device structure and are not yet fully understood.^[1b,2d]

Strontium titanate (SrTiO₃; STO), the archetypical perovskite oxide with a vast majority of functional properties and an incredible flexibility for functionalization through compositional and structural engineering,^[5] has shown great potential for nanoscale resistive switching applications.^[2a,c–e,6] This is due to the inherent tendency of the stable perovskite structure of STO to harbor oxygen vacancy point defects and the pronounced redox activity along the dislocations in Ti sub-lattice.^[2d,f] However, the high processing temperatures and non-CMOS compatible substrates typically employed in STO-based devices create a barrier to the commercialization of these devices.

The phenomena arising from the electromechanical coupling in perovskite oxides at low dimensions can facilitate novel approaches that can overcome current technological bottlenecks^[7] to realise the next generation of non-volatile memories and logic devices based on nanoionics enabled resistive switching effect.^[5b,8] Nanoscale electromechanical phenomena in functional oxide layers, ranging from flexoelectricity to mechanically-induced insulator-metal transitions (IMTs), have been a subject of rigorous research effort in recent years.^[8,9]

H. Nili, Dr. S. Walia, Dr. S. Balendhran,
Dr. M. Bhaskaran, Dr. S. Sriram
Functional Materials and Microsystems Research Group
School of Electrical and Computer Engineering
RMIT University
Melbourne, Victoria, Australia
E-mail: hussein.nili@rmit.edu.au;
sharath.sriram@rmit.edu.au

Prof. D. B. Strukov
Electrical and Computer Engineering Department
University of California Santa Barbara
Santa Barbara, CA 93106, USA



DOI: 10.1002/adfm.201401278

In case of STO, strain-induced effects (such as ferroelectricity) have been previously reported and investigated in detail.^[5d,10] Recent theoretical studies have also indicated the role of mechanical stress in enhancing in-plane oxygen vacancy migration.^[11] In situ electrical nanoindentation provides a powerful tool to investigate such phenomena in complex electronic material systems through providing a direct time-based coupling between nano-mechanical and electrical response.^[12]

Here, we present CMOS-compatible resistive switching devices, based on amorphous STO (*a*-STO) thin films synthesized at room temperature, with excellent resistive switching performance. Compositional analysis of the virgin (as-grown) and electroformed devices underpin the nanoionics-based processes responsible for the conduction mechanisms in *a*-STO switches. Further, nano-contact studies utilizing in situ electrical nanoindentation reveals the formation of uniformly distributed nano-filaments upon electroforming, each of which can act as individual nano-switches. We then utilized the technique to study in situ the conduction mechanisms in ultrathin *a*-STO thin films during the electroforming step and investigate the possible electromechanical coupling effects.

2. *a*-STO MIM Devices

Oxygen vacancy induced defect structures induced by electroforming play a decisive role in determining the resistive switching performance of metal-oxide-based devices. Therefore, synthesizing the oxide layer with a controlled concentration of oxygen vacancies can enhance the switching performance via the introduction of a network of point defects. Moreover, a built-in oxygen vacancy network provides greater flexibility and control over the electroforming process and partially eases high energy requirements for the creation of defect-rich, conductive filamentary pathways.

We have synthesized oxygen deficient amorphous STO (*a*-STO) thin films using RF magnetron sputtering at room temperature, which allows a precise control over the thickness of the oxide layer (down to 10 nm) and the oxygen deficiency concentration. X-ray photoelectron spectroscopy (XPS) depth profile results on as-grown *a*-STO thin films (in the virgin state, prior to electrical tests) reveal a uniform oxygen deficiency distribution throughout the thickness of the films (see Supporting Information Figure S1). As such, the controlled physical vapor deposition process eliminates the need for the high-temperature, reducing processing steps commonly required for the creation of oxygen vacancies in STO.^[2e,6b,13] To investigate the process of electroforming and subsequent electroresistive switching in *a*-STO oxide layers, micrometer scale (20–100 μm dimensions) asymmetric MIM switching cells using a 100 nm oxide layer were fabricated in Pt/Ti/*a*-STO/Pt configuration. Electrical characterization was performed by applying a bias voltage to the bottom or top electrode with the opposite electrode grounded (see Supporting Information Section S2). The initial current–voltage (*I*–*V*) curves of MIM devices in virgin state exhibited an area dependent, Schottky-like rectifying characteristic correlated with the choice of bias electrode and voltage polarity (see Supporting Information Figure S2a). The *I*–*V* characteristics confirm the expected formation of

dissimilar Schottky barriers at the Ti/*a*-STO and *a*-STO/Pt interfaces. A single irreversible electroforming (or forming) step, in form of a voltage sweep with maximum voltages in the range of |8–10| V, was required to trigger the electroresistive switching behavior in *a*-STO MIM devices (Figure 1a). The switching polarity of formed devices is governed by the relative voltage bias polarity between top and bottom electrodes during the electroforming step (see Supporting Information Section S2). Although top and bottom electrode biased devices were successfully electroformed with both bias polarities (see Supporting Information Figure S3), devices formed with an effective positive polarity at the bottom *a*-STO/Pt interface (either through applying a positive bias to the bottom electrode or a negative bias to the top electrode) exhibited greater yield with superior and stable switching performance, and therefore, are the focus of this study.

Post-electroforming, these devices exhibit stable non-volatile bipolar switching characteristics (Figure 1a,b) with OFF/ON ratios that exceed 10^3 over a wide range of READ voltages highlighting their operational flexibility (Figure 1c). Individual devices were successfully operated for more than 10^6 *I*–*V* sweep WRITE/ERASE cycles with less than 10% deviation in the switching voltages (Figure 1c). No appreciable change in the high resistance state (HRS) and low resistance state (LRS) properties was observed at a read voltage of ± 250 mV in either polarity over repeated reading cycles of 10^5 seconds (<1% over the total READ period). Pulsed WRITE/READ/ERASE cycles were carried out using pulse widths of 1–100 μs with a rise time of 50 ps. Table 1 outlines the switching performance of *a*-STO cells from over a hundred tested devices. Both READ and WRITE operations can be carried out at very low current density (considering the cell sizes) in micro-meter scale *a*-STO devices.

The bipolar switching behavior of transition metal oxide layers in MIM configuration is generally perceived to be originating from inhomogeneous conduction mechanisms through localized filamentary channels.^[1a,4,14] As such, the current transport in HRS and LRS regimes is expected to be independent of the geometric area of the MIM device. Figure 1d presents the resistance-area product vs. the device area for micron-sized *a*-STO MIM cells of various sizes. The increase in the *R* \times *A* product with increasing the device size clearly indicates a local conduction mechanism in both HRS and LRS regimes.^[4b] Further, No appreciable size-dependency was observed for either the ON/OFF ratios or the READ/WRITE current densities in either state. The size-independency calls for a detailed investigation into the nature of resistive switching mechanisms in *a*-STO devices which will be addressed in the following sections, as this is an invaluable trait for scaling devices down to the nanoscale.

The switching performance of *a*-STO devices is comparable to the best reported STO and TiO₂ based devices.^[4,14] Moreover, to the best authors' knowledge, such switching performance has not been previously demonstrated in STO-based devices on CMOS-compatible substrates (most reported devices have been fabricated on single crystal STO substrates)^[2e,15] or with a low temperature CMOS-compatible process. The facile fabrication of high performance resistive switching devices based on a single *a*-STO oxide layer can open new horizons in design and fabrication of resistive memory devices complementary to

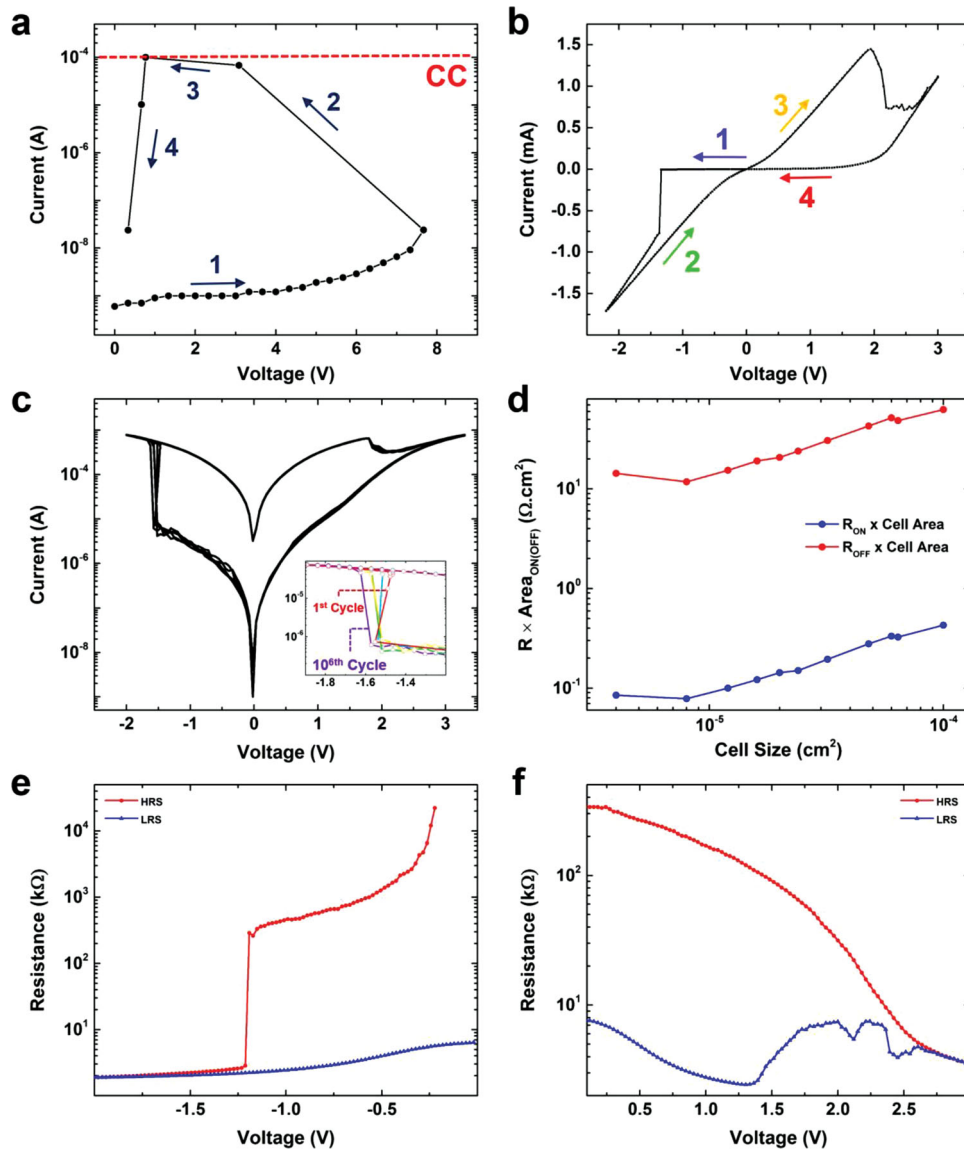


Figure 1. Resistive switching performance of electroformed *a*-STO MIM cells. a) Typical electroforming sweep in positive polarity for *a*-STO MIM cells biased from the bottom electrode. b) Typical bipolar switching behavior of *a*-STO MIM cells. c) Bipolar switching performance of a single cell over 10^6 consecutive *I*-*V* sweep cycles. Resistance-area products for *a*-STO MIM cells of various sizes in OFF and ON states. The resistance values were extracted through a linear fit to the *I*-*V* curves in the range of designated READ voltages of ± 250 mV. e) High and f) low resistance states (HRS and LRS, respectively) of *a*-STO cells as function of READ voltage.

Table 1. Performance characteristics of *a*-STO memory cells.

Write Voltage/Current [V/ μ A]	-1.35/200
Read Voltage/Current at LRS [mV/ μ A]	$\pm 250/85$
Erase Voltage/Current [V/ μ A]	1.9/600
Read Voltage/Current at HRS [mV/ μ A]	$\pm 250/0.6$
Retention [s]	$>10^5$
Number of Cycles	$>10^6$
ON Switch Voltage Drift	$8.6 \pm 1\%$
OFF Switch Voltage Drift	$4.5 \pm 1\%$

planar, semiconductor technology in the form of biocompatible and flexible devices.^[16]

2.1. Electroforming Mechanism

The electroforming process facilitates the electroresistive switching in intrinsically insulating metal oxides by permanently altering their stoichiometry and oxygen vacancy distribution via redox processes.^[2c,f,6b] In order to characterize the impact of electroforming on the defect chemistry of *a*-STO thin films, XPS depth profile was performed on $100 \mu\text{m} \times 100 \mu\text{m}$

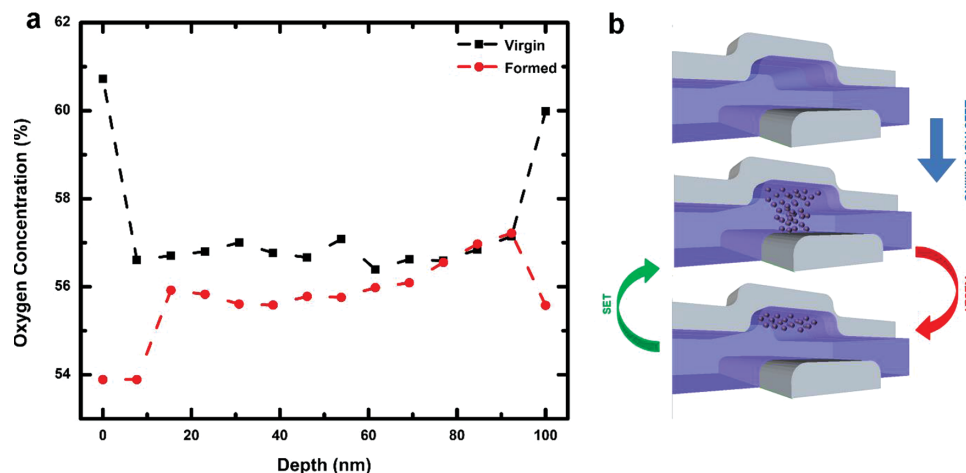


Figure 2. Electroforming and switching mechanisms in *a*-STO MIM cells. a) Relative oxygen concentration throughout the thickness of the oxide layer calculated based on XPS depth profile results on $100\ \mu\text{m} \times 100\ \mu\text{m}$ cells. b) Schematic of electroforming and subsequent switching mechanisms in *a*-STO cells. The electroforming step results in an enhanced oxygen deficiency in the MIM cell. Subsequent motion of oxygen ions along the extended defect structure is responsible for bi-stable, cyclic switching behaviour.

junctions before and after electroforming (see Supporting Information Figure S2 for the details of electroforming step). The devices size was chosen to comply with the lowest X-ray spot-size ($100\ \mu\text{m}$) available in the XPS system (see Supporting Information Section S3). Virgin devices exhibit a largely uniform atomic concentration with an oxygen deficiency of $\approx 3\%$ indicating a weak n-type doping (Figure 2a). On the other hand, electroformed devices show an overall enhancement in oxygen deficiency concentration ($\approx 5\%$), in particular a sharp increase at the top interface with the titanium layer (Figure 2a). However, due to the averaging nature of the technique, an increase in the oxygen deficiency of the formed relative to the virgin devices implies that a large area of device has undergone redox processes upon electroforming. This is in contrast to common observations of highly localized filamentary pathways (usually around the edges) in MIM resistive switching devices based on redox processes in metal oxides (for example, in TiO_2 and Fe-SrTiO_3).^[14,17] This instigated further investigation into the impact of electroforming on the structure and switching mechanisms of *a*-STO devices using in situ nanoscale probing experiments in the following sections.

Since the oxygen deficiency distribution is uniform in the virgin oxide layer, the metal/oxide interfaces dominate the conduction mechanisms in virgin devices and therefore largely govern the electroforming process. At a sufficiently high voltage bias, an abrupt jump in current is observed. A current compliance limit of $100\ \mu\text{A}$ ensures that the bias voltage is compensated (i.e., scaled back) to prevent further breakdown of the device. Following this process, the devices exhibit repeatable bipolar switching behavior between a highly conductive ON and a highly resistive rectifying OFF state. This denotes electrically induced redox processes taking place at the Ti/*a*-STO interface which create a locally high concentration of oxygen vacancies in the vicinity of metal/oxide interface,^[2f] during the electroforming process with the *a*-STO/Pt interface as the drive (anode) electrode. Subject to a high electrical gradient, oxygen vacancies drift away from the forward biased bottom interface through the most favorable paths in

the amorphous oxide structure towards the top Ti/*a*-STO interface, resulting in a strongly n-type doped region with a high concentration of oxygen vacancies in the vicinity of the top interface. This in turn lowers the electronic barrier at the top interface, facilitating the redox processes under the high electrical stress. As such, the electrical barrier at top Ti/*a*-STO interface irreversibly collapses, and conductive channels propagate towards the bottom *a*-STO/Pt interface, creating a virtual cathode which is limited by the current compliance limit and the forward bias on the anode.^[2f,4a]

2.2. Nanoionics Switching Mechanisms

Figure 2b depicts a schematic for the switching behaviour of *a*-STO cells after the electroforming step. The electroformed *a*-STO MIM devices are pre-set to ON state. The switching behaviour of electroformed *a*-STO MIM cells can be described by a simplistic memristor plus rectifier equivalent circuit.^[4a] In the OFF state, the conduction mechanism of the device is governed by the low oxygen vacancy concentration region at the bottom *a*-STO/Pt interface (the current limiting anode) as indicated by the rectifying Schottky-like transport characteristics of the I - V curves (Figure 1b). On applying a negative bias to the bottom interface, oxygen vacancies drift from the ohmic virtual cathode region (vacancy enriched Ti/*a*-STO interface) towards the bottom electrode through the pre-formed conduction channels, thinning the depletion layer at the *a*-STO/Pt interface and switching the device to ON state where the electron tunneling through a thin residual barrier manifests itself as a symmetrical I - V characteristic^[4a] (Figure 1). This can be attributed to the electrons tunneling through the thin residual barrier at the top interface similar for TiO_2 devices (reported by Yang et al.^[4]). A reversal of bias polarity at the bottom interface repels the oxygen vacancies in the conduction channel(s) further away from the *a*-STO/Pt interface resulting in the recovery of the electronic barrier and switching the device back to OFF state.

3. Nano-Contact Electromechanical Investigations of *a*-STO Thin Films

The evolution of conductive channels due to field-dependent non-linear ionic migration along the network of point defects in *a*-STO thin films appears to play a decisive role in the switching behavior of *a*-STO-based cells. However, it is difficult to isolate the individual contributions of the oxide layer and the electrode interfaces towards the overall conduction mechanisms that occur during the electroforming and bipolar switching events in MIM structures. To this end, in situ electrical nanoindentation can be employed as a powerful characterization tool as it provides stable nanoscale contacts with extremely accurate real-time control over the contact size (<5 nm in both axial and lateral dimensions) and pressure.^[12,18] Moreover, the unrivaled mechanical load control in nanoindentation experiments and precise time-based correlation between mechanical and electrical responses make it the premium tool to study strain-induced phenomena at the nanoscale.^[12a,b,18]

We employed in situ electrical nanoindentation technique to acquire fundamental insights into the nanoionics-based conduction mechanisms in *a*-STO based devices using a conductive Berkovich tip. Throughout these in situ measurements, the underlying platinum substrate was uniformly forward-biased while a progressively increasing nanoscale contact area (as a function of applied force) at the surface of thin film was grounded.

Accurate assessment of the in situ electrical nanoindentation data, requires a careful characterization of the electromechanical properties of nano-contacts formed through the conductive Berkovich probe. The inherent electrical and mechanical properties of the conductive Berkovich tip as well as the resistance imposed by the probe contact on the nano-contact area have been thoroughly assessed on standard quartz and conductive metallic samples (see Supporting Information Section S5). The empirical relations for the nano-contact resistance derived based on these assessments, allow to characterize and separate the effects of probe's resistance, surface adsorbates and contaminations and surface roughness effects on the contact resistance in elastic and elasto-plastic nanoindentation contacts.

3.1. Nano-Contact Studies of the Conduction Mechanisms in *a*-STO MIM Cells

Virgin and formed *a*-STO devices were investigated using nanoscale contacts with the conductive indentation probe to clarify their switching behavior. The electrical properties of the nano-contacts formed by the conductive indenter probe were characterized on standard metallic substrates (see Supporting Information Figure S5). Top metal electrodes (50/10 nm Pt/Ti layer) were removed from $2\ \mu\text{m} \times 2\ \mu\text{m}$ areas of different-sized devices via a precise depth limited scanning wear step. **Figures 3a,b** show the in situ scanning probe microscopy (SPM) scans on the surface of virgin and formed *a*-STO devices under the top electrode. The cluster-like nano-grains (average diameter of ≈ 80 nm) are distributed uniformly under the electrode in the formed devices (in both switching states).

Nanoscale probing of the electroformed devices was carried out using an indentation force of 100 μN with a ± 250 mV voltage sweep at the maximum load (equivalent contact diameter $d \approx 80$ nm). **Figure 3b,c** illustrate a device area before and after indentation experiments. The nano-mechanical response of the non-deformed regions under a 100 μN indentation load is almost fully elastic. In contrast, the large plastic deformation of the nano-grains under identical loads indicate a weak mechanical structure for the nano-grains (**Figure 3d**). Further, the non-deformed regions show an insulating behavior upon sweeps at maximum load, similar to that of the virgin devices (**Figure 3e**), whereas a bi-stable switching current transport (with an average current density of 50 A/cm^2) is observed for the nano-grains (**Figure 3f**). As such, structurally weak nano-grains with a bi-stable switching behavior can in fact be regarded as the filamentary pathways throughout the oxide layer in *a*-STO devices. These “nano-filaments” are distributed uniformly over the device area, contributing to the bipolar switching behavior as a parallel network. Hence, the overall increase in the oxygen vacancy concentration throughout the thickness of switching devices as characterized by XPS depth profile results (**Figure 2**) denotes the formation of uniformly distributed nano-filaments upon electroforming. Previous studies into the nature of conductive filamentations in redox based resistive switching devices have typically identified localized filamentary pathways in electroformed devices.^[14,17] Some researchers have reported evidence of homogenous conductivity in the ON state in Fe-STO thin films^[2d,e] as well as individually switchable localized point defects at single dislocations on the surface of STO single crystals.^[6b,15c,19] However, such highly localized individually switchable nano-filaments have not been previously reported in metal-oxide MIM cells. The formation of these isolated “nano-switches” has to do with the amorphous nature of the functional metal oxide. While a pre-existing point-defect structure in the amorphous network facilitates the formation of filamentary pathways during the electroforming, lack of crystalline order results in a non-preferential expansion of isolated defects and effectively limits the extended defect structures to a close neighbourhood of the initial point defects. These observations signal the great potential of *a*-STO cells in terms of scalability and energy requirements for switching operations. The small dimensions and the uniform distribution of individual nano-switches indicate the ultimate scalability of these devices and low voltage/current requirements for their READ/WRITE operations qualifies them further for large area integration as memory devices.

3.2. Formation of Conductive Channels at Nano-Contacts: Strain Effect

In situ electrical nanoindentation is used to investigate in detail the nanoscale dynamics of conduction mechanisms in *a*-STO/Pt stacks. As-grown *a*-STO thin films (100, 60, and 12 nm) were found to be completely insulating when probed using ultra low load nano-contacts (equivalent contact diameter $d = 80$ nm). 100 and 60 nm thin films were then subjected to a series of high voltage sweeps at progressively increasing (from 0.1 to 5 mN) indentation loads. Throughout

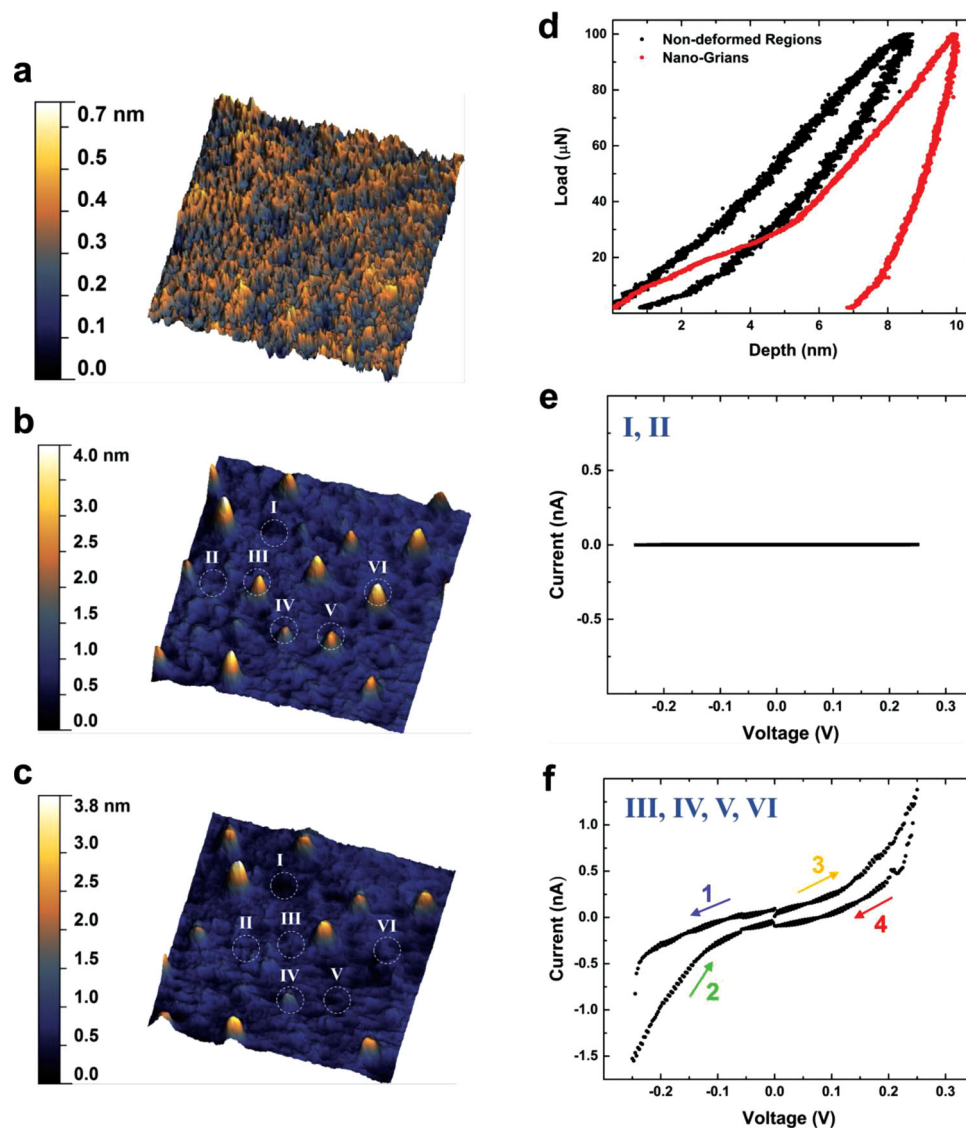


Figure 3. In situ SPM scans ($1 \mu\text{m} \times 1 \mu\text{m}$) and electrical nanoindentation on *a*-STO MIM cells after removing the top Pt/Ti electrodes (top Ti/*a*-STO interface). a) In situ SPM scan of *a*-STO oxide surface in a virgin cell. b,c) In situ SPM scans of electroformed *a*-STO oxide surfaces before and after in situ electrical indentation with a $100 \mu\text{N}$ force (equivalent contact diameters of 80 nm), respectively. d) Load-displacement curves of the non-deformed surface and nano-grains in electroformed *a*-STO cells. e) Insulating current transport behaviour of non-deformed regions (I and II). f) The repeatable bi-stable switching of individual nano-grains (III to VI).

these experiments, the nano-mechanical response of *a*-STO thin films was monitored to ensure the ultimate nano-contact depth does not breach the film's thickness (see Supporting Information Section S6). A stable Schottky transport behaviour was observed for *a*-STO/Pt stacks at stable contact loads up to 1 mN . A dramatic non-linear increase in current density is observed at higher indentation loads ($>1 \text{ mN}$) after accounting for the increased contact area and the non-uniform resistivity of the indenter tip contact (Figure 4a). Moreover, SPM scans of high-load nanoscale contact areas revealed deformations around the contact area for contact loads $\geq 1 \text{ mN}$ as a direct consequence of the voltage sweep cycles (Figure 4b–d).

Low-load nano-contact probing of the deformed regions reveals a significant uniform enhancement in electrical

conductivity (Figure 4e) indicating the creation of conductive paths inside the oxide layer. Based on these observations, two principal strain-related phenomena can be identified. Firstly, increasing the contact load results in a corresponding decrease in the width of the depletion layer at the *a*-STO/Pt interface. This is presumably the result of enhanced carrier concentration due to increased defect density. More importantly, the application of mechanical force enhances the drift-diffusion of oxygen vacancies in the *a*-STO network.^[11b] Due to the geometry of the nano-contact (defined by the non-ideal geometry of the Berkovich probe and the nano-mechanical deformation of *a*-STO thin films), the majority of the electrical contact area is concentrated at the peripheral nano-contact area (rather than its center) where the number of contact asperities is larger and the topographical profiles of the contacting sides

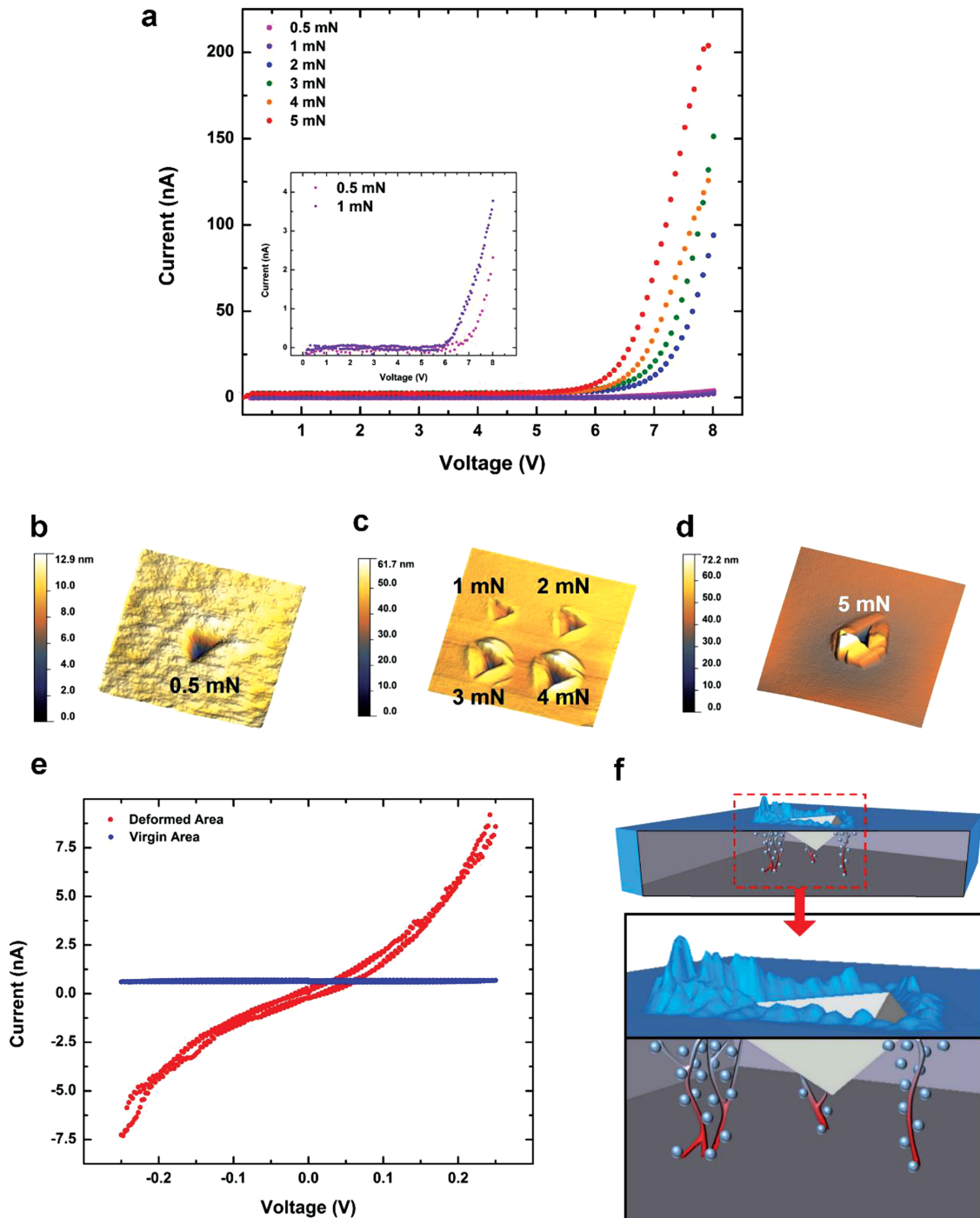


Figure 4. Electrical transport behavior and structural deformations in 60 nm *a*-STO/Pt stacks subject to in situ electrical nanoindentation experiments. a) Current transport behavior of 60 nm *a*-STO films under increasing nanoindentation loads. b–d) SPM scans of deformations around the electrical nano-contact area in 60 nm *a*-STO films under different loads after 10 cycles of high voltage sweeps under increasing maximum indentation loads. The scan area is $1 \mu\text{m} \times 1 \mu\text{m}$ in (b) and $5 \mu\text{m} \times 5 \mu\text{m}$ in both (c) and (d). e) Current transport of virgin and deformed regions (around the 5 mN contact area, after sweep cycles) in 60 nm *a*-STO thin films. f) Schematic of formed filaments as a result of oxygen vacancies migration around the nano-contact area.

are smoother. Therefore, oxygen vacancies diffuse towards the peripheral electrical contacts in the nano-contact area through the network of pre-existing point defects, forming conductive filamentary channels *via* the creation of extended defect structures (Figure 4f).

3.3. Direct Electroforming at *a*-STO/Pt Interface

Nano-contact investigations were conducted on ultra-thin (12 nm) *a*-STO films to investigate the role of oxide/metal interfaces in the electroforming and switching behaviors. At

such small thicknesses the short range electronic effects at the *a*-STO/Pt anode interface can be closely mimicked. Moreover, at such low dimensions the higher local densities of the point defects augment the impact of electromechanical stimuli on the interfacial electronic properties as well as the non-linear ionic transport in *a*-STO layers. Probed with ultra low-load (50-100 μ N) nano-contacts, these ultra-thin films exhibited a fully elastic mechanical behaviour and consistently maintained their highly insulating virgin characteristics (see Supporting Information Figure S8) which are governed by the Schottky effect that arises due to the depletion region at the *a*-STO/Pt interface. The effect of the mechanical pressure on the transport characteristics of the interface were observed even at such small loads (see Supporting Information Figure S8b). On the other hand, high voltage (up to 10 V) sweeps at 250 and 500 μ N contact loads (corresponding contact diameters of 100 of 130 nm respectively) result in an abrupt deviation from the Schottky behavior of the transport characteristics of the metal-oxide interface (Figure 5a,b). The critical threshold voltage is found to be proportional to the contact load. Moreover, the change in the current transport characteristics is accompanied by large displacement of the nano-contact and chaotic

deformations in a large area around the contact area. (Figure 5c,d). At voltages above the threshold value, the current transport characteristics resemble space charge limited conduction (SCLC) at the *a*-STO/Pt interface.

Such transport mechanisms require low barrier heights (e.g., a metal- n^+ oxide interface) for easy charge carrier injections into the conduction band of the oxide.^[20] Conductive mappings of the deformed regions utilizing low load nano-contacts (100 μ N contact loads) reveal a full spectrum of conduction behaviors at localized areas in the deformed region (Figure 6). This pattern indicates the localized changes in the interfacial electronic barrier and the formation of conductive pathways through the oxide layer. These observations help complete the picture of the electroforming process dynamics and subsequent switching mechanisms in *a*-STO resistive switches and further signify the assistive role of mechanical pressure in such mechanisms.

The mechanical pressure reduces the thermodynamical requirements for the drift-diffusion of frozen-in vacancy point defects in the oxide layer. As a result, subject to a sufficiently high electric field gradient, mechanically assisted local redox processes render the oxide layer around the nano-contact area

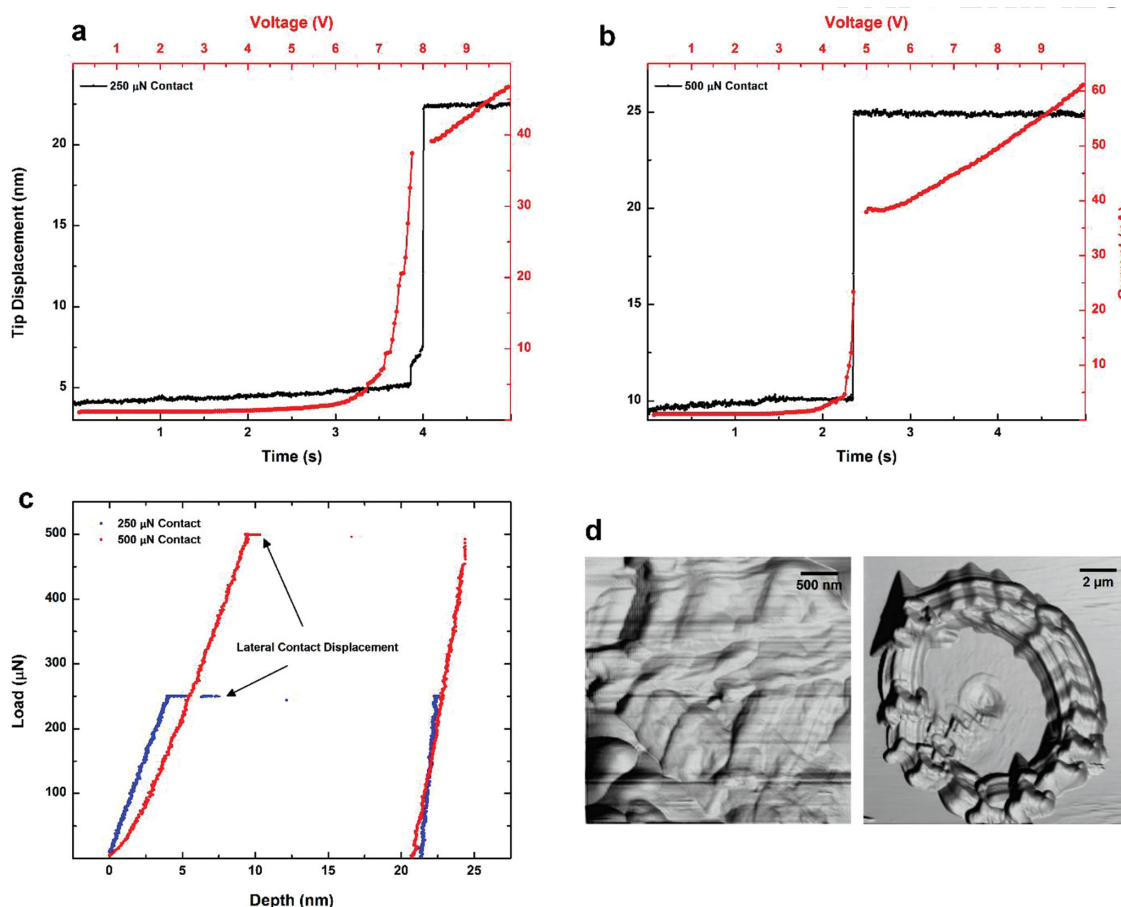


Figure 5. Current transport at the 12 nm *a*-STO/Pt interface at 250 and 500 μ N contact loads. a,b) The time/voltage correlation of abrupt changes in the *I*-*V* characteristics and contact displacements at constant contact loads upon 10 V voltage sweeps. c) Load-displacement curves of the 250 and 500 μ N nano-contacts highlighting the lateral displacement of the nano-contact at constant loads upon high voltage sweeps. d) Zoomed-in and large-area SPM scans of the deformed regions around the 500 μ N nano-contact as a result of the high voltage sweeps.

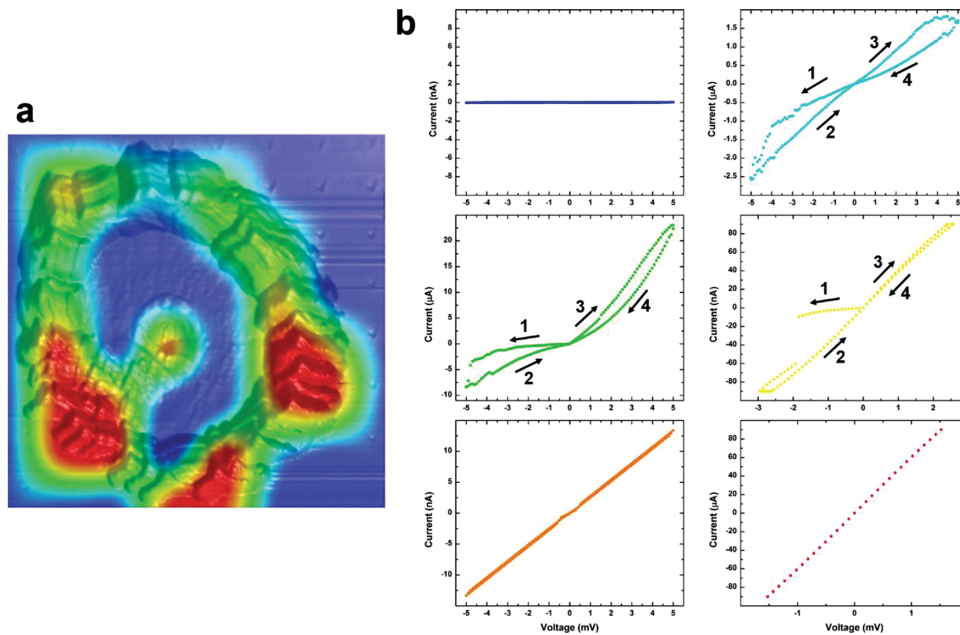


Figure 6. Conduction and switching characteristics of 12 nm *a*-STO/Pt stacks after direct electroforming with nanoindentation contacts. a) Contour map of areas with distinct conduction characteristics in deformed 12 nm *a*-STO thin films. b) Individual *I*-*V* characteristics of different regions in the deformed area (colors correspond to those of the contours map for deformed regions). Non-deformed regions retain their highly insulating properties. In the deformed region, the partial formations of strong and weak conductive channels result in distinct resistive states. Ohmic regions with high current densities are the result of a complete breakdown of electronic barrier and the formation of strong conductive filaments.

into a highly n-type conducting state which in effect changes the electronic nature of the metal-oxide interface. Moreover, redox processes induce locally formed conductive filaments with distinct current transport characteristics.

4. Conclusion

Amorphous STO (*a*-STO) thin films with controllable as-grown oxygen deficiency induced defect structures were synthesized through a facile low-temperature PVD process. Pt/Ti/*a*-STO/Pt MIM cross-point devices exhibited exceptional bipolar switching performance subsequent to a single electroforming step the polarity of which can govern the switching polarity of *a*-STO cells. Consistently high switching ratios in the order of 10^3 – 10^4 were observed at small READ voltage/current. Nano-contact studies of *a*-STO MIM devices reveals that the electroforming step results in the formation of uniformly distributed conductive nano-filaments in the oxide layer. Each of these filaments are switchable in isolation and thus act as individual resistive nano-switches. The in situ electrical nanoindentation experiments on *a*-STO/Pt stacks confirm the underlying electronic and ionic transport phenomena that take place during the electroforming and highlight the impact of mechanical stress on the modulation of non-linear ionic transport mechanisms in *a*-STO films. Ultra-thin *a*-STO films were directly electroformed using nano-scale contacts with controlled mechanical load. The resulting conductive filamentary regions exhibited distinct current transport and switching characteristics. These insights promise that perovskite memristors hold the key for high performance memristive systems.

5. Experimental Section

Oxygen Deficient *a*-STO Thin Films: 100, 60, and 12 nm amorphous SrTiO₃ (*a*-STO) thin films with as-grown oxygen deficiencies were deposited on Pt/TiO₂/SiO₂ (50:10:300 nm) coated Si substrates using RF magnetron sputtering at room temperature, from a stoichiometric ceramic target. Thin films were sputtered in a pure argon atmosphere with a sputtering pressure of 5 mTorr (from a base pressure $<10^{-7}$ Torr).

***a*-STO Crossbar Devices:** Microscale *a*-STO crossbar arrays were fabricated on SiO₂/Si substrates using a three-step photolithography/lift-off process. In the first lift-off step, 50 nm bottom platinum electrodes with 10 nm TiO₂ adhesion layers were deposited on pre-patterned SiO₂/Si substrates by electron beam evaporation at room temperature. Oxygen deficient *a*-STO thin films of 100 nm thickness were then RF sputtered through a shadow mask. Lastly, Pt/Ti (50:10 nm) top electrodes were patterned using photolithography deposited by electron beam evaporation at room temperature through to complete the crossbar structure.

Electrical Characterization of Cross-Bar Devices: The electrical characterization of *a*-STO crossbar devices was performed using an Agilent 2912A sourcemeter for two-probe direct current and pulse transient measurements. Characterizations were performed using either the bottom or top electrode as the drive electrode with the opposite electrode connected to the system ground.

X-Ray Photoelectron Spectroscopy: X-ray photoelectron spectroscopy (XPS) surface and depth profile analyses were carried out using a Thermo Scientific K-Alpha instrument. An aluminium K α radiation source with energy of 1485 eV was used, with the adventitious carbon peak (at 284.8 eV) used as the calibration reference for fitting of the core level spectra of the principal elements. The composition of the films was determined utilizing the area under the curves, fitted, and corrected with sensitivity factors using the Avantage data system. Depth profiling was performed by successive, cyclic argon-ion etch and spectral acquisition processes.

In Situ Electrical Nanoindentation: Nanoindentation experiments with in situ electrical measurements were carried out using Hysitron's

NanoECR system on a TI 950 Tribointender. A conductive Pulsar Berkovich tip was used, with the nanoindentation technique enabling the in situ measurement of electrical contact resistance between the indenter tip and the specimen. Extra care was taken into account to minimize the effects of surface adsorbates and contaminations by extensively cleaning both the samples and the conductive probe (ultrasonic cleaning using organic solvents and blow drying with dry nitrogen) prior to the experiments. Details of the experimental setup and measurement procedures can be found in our previous reports.^[12]

Supporting Information

Supporting Information is available from the Wiley Online Library or from the author.

Acknowledgements

The authors acknowledge the Australian Research Council for funding in the form of project (DP130100062), fellowship (DP1092717 and DP110100262), and infrastructure (LE0882246, LE0989615, and LE110100223) support.

Received: April 21, 2014

Revised: June 13, 2014

Published online:

- [1] a) D. B. Strukov, H. Kohlstedt, *MRS Bull.* **2012**, *37*, 108; b) J. J. S. Yang, D. B. Strukov, D. R. Stewart, *Nat. Nanotechnol.* **2013**, *8*, 13.
- [2] a) A. Sawa, *Mater. Today* **2008**, *11*, 28; b) D. B. Strukov, G. S. Snider, D. R. Stewart, R. S. Williams, *Nature* **2008**, *453*, 80; c) R. Waser, M. Aono, *Nat. Mater.* **2007**, *6*, 833; d) R. Dittmann, R. Muenstermann, I. Krug, D. Park, T. Menke, J. Mayer, A. Besmehn, F. Kronast, C. M. Schneider, R. Waser, *Proc. IEEE* **2012**, *100*, 1979; e) R. Muenstermann, T. Menke, R. Dittmann, R. Waser, *Adv. Mater.* **2010**, *22*, 4819; f) R. Waser, R. Dittmann, G. Staikov, K. Szot, *Adv. Mater.* **2009**, *21*, 2632.
- [3] D. B. Strukov, J. L. Borghetti, R. S. Williams, *Small* **2009**, *5*, 1058.
- [4] a) J. J. Yang, M. D. Pickett, X. M. Li, D. A. A. Ohlberg, D. R. Stewart, R. S. Williams, *Nat. Nanotechnol.* **2008**, *3*, 429; b) H. Kohlstedt, A. Petraru, K. Szot, A. Rudiger, P. Meuffels, H. Haselier, R. Waser, V. Nagarajan, *Appl. Phys. Lett.* **2008**, *92*, 62907.
- [5] a) R. Merkle, J. Maier, *Angew. Chem. Int. Ed.* **2008**, *47*, 3874; b) J. M. Rondinelli, S. J. May, J. W. Freeland, *MRS Bull.* **2012**, *37*, 261; c) A. F. Santander-Syro, O. Copie, T. Kondo, F. Fortuna, S. Pailhes, R. Weht, X. G. Qiu, F. Bertran, A. Nicolaou, A. Taleb-Ibrahimi, P. Le Fevre, G. Herranz, M. Bibes, N. Reyren, Y. Apertet, P. Lecoeur, A. Barthelemy, M. J. Rozenberg, *Nature* **2011**, *469*, 189; d) P. Zubko, G. Catalan, A. Buckley, P. R. L. Welche, J. F. Scott, *Phys. Rev. Lett.* **2007**, *99*, 4; e) S. Walia, S. Balendhran, H. Nili, S. Zhuiykov, G. Rosengarten, Q. H. Wang, M. Bhaskaran, S. Sriram, M. S. Strano, K. Kalantar-zadeh, *Prog. Mater. Sci.* **2013**, *58*, 1443.
- [6] a) S. Menzel, M. Waters, A. Marchewka, U. Bottger, R. Dittmann, R. Waser, *Adv. Funct. Mater.* **2011**, *21*, 4487; b) K. Szot, W. Speier, G. Bihlmayer, R. Waser, *Nat. Mater.* **2006**, *5*, 312; c) J. Hou, S. S. Nonnenmann, W. Qin, D. A. Bonnell, *Adv. Funct. Mater.* **2014**, n/a.
- [7] H. Schroeder, V. V. Zhirnov, R. K. Cavin, R. Waser, *J. Appl. Phys.* **2010**, *107*, 8.
- [8] Y. Kim, S. J. Kelly, A. Morozovska, E. K. Rahani, E. Strelcov, E. Eliseev, S. Jesse, M. D. Biegalski, N. Balke, N. Benedek, D. Strukov, J. Aarts, I. Hwang, S. Oh, J. S. Choi, T. Choi, B. H. Park, V. B. Shenoy, P. Maksymovych, S. V. Kalinin, *Nano Lett.* **2013**, *13*, 4068.
- [9] a) Y. Kim, A. N. Morozovska, A. Kumar, S. Jesse, E. A. Eliseev, F. Alibart, D. Strukov, S. V. Kalinin, *ACS Nano* **2012**, *6*, 7026; b) T. D. Nguyen, S. Mao, Y. W. Yeh, P. K. Purohit, M. C. McAlpine, *Adv. Mater.* **2013**, *25*, 946.
- [10] a) N. A. Pertsev, A. K. Tagantsev, N. Setter, *Phys. Rev. B* **2000**, *61*, R825; b) J. H. Haeni, P. Irvin, W. Chang, R. Uecker, P. Reiche, Y. L. Li, S. Choudhury, W. Tian, M. E. Hawley, B. Craigo, A. K. Tagantsev, X. Q. Pan, S. K. Streiffer, L. Q. Chen, S. W. Kirchoefer, J. Levy, D. G. Schlom, *Nature* **2004**, *430*, 758; c) H. W. Jang, A. Kumar, S. Denev, M. D. Biegalski, P. Maksymovych, C. W. Bark, C. T. Nelson, C. M. Folkman, S. H. Baek, N. Balke, C. M. Brooks, D. A. Tenne, D. G. Schlom, L. Q. Chen, X. Q. Pan, S. V. Kalinin, V. Gopalan, C. B. Eom, *Phys. Rev. Lett.* **2010**, *104*, 4.
- [11] a) R. Al-Hamadany, J. P. Goss, P. R. Briddon, S. A. Mojarad, M. Al-Hadidi, A. G. O'Neill, M. J. Rayson, *J. Appl. Phys.* **2013**, *113*, 8; b) R. Al-Hamadany, J. P. Goss, P. R. Briddon, S. A. Mojarad, A. G. O'Neill, M. J. Rayson, *J. Appl. Phys.* **2013**, *113*, 8.
- [12] a) H. Nili, K. Kalantar-zadeh, M. Bhaskaran, S. Sriram, *Prog. Mater. Sci.* **2013**, *58*, 1; b) M. Bhaskaran, S. Sriram, S. Ruffell, A. Mitchell, *Adv. Funct. Mater.* **2011**, *21*, 2251; c) H. Nili, G. Cheng, T. Venkatesh, S. Sriram, M. Bhaskaran, *Mater. Lett.* **2013**, *90*, 148.
- [13] a) G. Herranz, M. Basletic, O. Copie, M. Bibes, A. N. Khodan, C. Carretero, E. Tadra, E. Jacquet, K. Bouzehouane, A. Hamzic, A. Barthelemy, *Appl. Phys. Lett.* **2009**, *94*, 3; b) T. Menke, P. Meuffels, R. Dittmann, K. Szot, R. Waser, *J. Appl. Phys.* **2009**, *105*, 3.
- [14] J. J. Yang, F. Miao, M. D. Pickett, D. A. A. Ohlberg, D. R. Stewart, C. N. Lau, R. S. Williams, *Nanotechnology* **2009**, *20*, 9.
- [15] a) K. Shibuya, R. Dittmann, S. B. Mi, R. Waser, *Adv. Mater.* **2010**, *22*, 411; b) S. Stille, C. Lenser, R. Dittmann, A. Koehl, I. Krug, R. Muenstermann, J. Perlich, C. M. Schneider, U. Klemradt, R. Waser, *Appl. Phys. Lett.* **2012**, *100*, 4; c) C. Rodenbucher, W. Speier, G. Bihlmayer, U. Breuer, R. Waser, K. Szot, *New J. Phys.* **2013**, *15*, 14.
- [16] P. Gutruf, C. M. Shah, S. Walia, H. Nili, A. S. Zoolfakar, C. Karnutsch, K. Kalantar-zadeh, S. Sriram, M. Bhaskaran, *NPG Asia Mater.* **2013**, *5*, 7.
- [17] a) D. H. Kwon, K. M. Kim, J. H. Jang, J. M. Jeon, M. H. Lee, G. H. Kim, X. S. Li, G. S. Park, B. Lee, S. Han, M. Kim, C. S. Hwang, *Nat. Nanotechnol.* **2010**, *5*, 148; b) R. Munstermann, J. J. Yang, J. P. Strachan, G. Medeiros-Ribeiro, R. Dittmann, R. Waser, *Phys. Status Solidi-Rapid Res. Lett.* **2010**, *4*, 16; c) F. Miao, J. P. Strachan, J. J. Yang, M. X. Zhang, I. Goldfarb, A. C. Torrezan, P. Eschbach, R. D. Kelley, G. Medeiros-Ribeiro, R. S. Williams, *Adv. Mater.* **2011**, *23*, 5633.
- [18] a) R. Nowak, D. Chrobak, S. Nagao, D. Vodnick, M. Berg, A. Tukiainen, M. Pessa, *Nat. Nanotechnol.* **2009**, *4*, 287; b) A. M. Minor, S. A. S. Asif, Z. W. Shan, E. A. Stach, E. Cyrankowski, T. J. Wyrobek, O. L. Warren, *Nat. Mater.* **2006**, *5*, 697.
- [19] A. Shkabko, M. H. Aguirre, A. Kumar, Y. Kim, S. Jesse, R. Waser, S. V. Kalinin, A. Weidenkaff, *Nanotechnology* **2013**, *24*, 9.
- [20] a) G. W. Dietz, W. Antpohler, M. Klee, R. Waser, *J. Appl. Phys.* **1995**, *78*, 6113; b) P. C. Joshi, S. B. Krupanidhi, *J. Appl. Phys.* **1993**, *73*, 7627.